

**Entropy-controlled fully reversible nanostructure formation of Ge on miscut vicinal Si(001) surfaces**Christian Grossauer<sup>1</sup>, Vaclav Holy<sup>2</sup>, and Gunther Springholz<sup>1,\*</sup><sup>1</sup>*Institut für Halbleiter- und Festkörperphysik, Johannes Kepler University, A-4040 Linz, Austria*<sup>2</sup>*Department of Condensed Matter Physics, Charles University, 121 16 Praha 2, and Department of Condensed Matter Physics, Masaryk University, 611 37 Brno, Czech Republic*

(Received 13 February 2020; revised 7 July 2020; accepted 16 June 2020; published 10 August 2020)

Entropy effects substantially modify the growth of self-assembled Ge nanostructures on vicinal Si(001) surfaces, on which one-dimensional nanowire-like structures are formed. As shown by variable temperature scanning tunneling microscopy, these nanostructures are not only tunable in size and shape, but can be fully reversibly erased and reformed without changes in sizes and composition. This unprecedented behavior is caused by the strong free surface energy renormalization due to the large step entropy of vicinal surfaces that strongly increases with increasing temperature. This favors a planar two-dimensional surface at higher temperatures in thermodynamic equilibrium, whereas the nanostructured surface is the preferred low-temperature configuration. Taking the step entropy into account, the critical transition temperature between these surface states derived by free-energy minimization is shown to scale nearly linearly with the Ge coverage—in excellent agreement with the experiments. Most importantly, the nanowire sizes are found to be deterministically controlled by the Ge thickness and vicinal angle, independently of the growth or annealing conditions. Thus, highly reproducible structures with tunable nanogeometries and -dimensions are obtained, which opens promising avenues for device applications.

DOI: [10.1103/PhysRevB.102.075420](https://doi.org/10.1103/PhysRevB.102.075420)**I. INTRODUCTION**

Self-assembled semiconductor nanostructures produced by strained-layer heteroepitaxy exhibit fascinating features and vast potentials for quantum electronic devices [1–7]. Their formation is typically based on the fundamental instability of strained layers against surface corrugations or three-dimensional (3D) island formation, driven by effective strain relaxation allowed by the unconstrained side faces [8–12]. This generic process leads to a substantial lowering of the total energy and thus occurs for a wide range of material systems [8–13]. As a result, a rich variety of sizes and shapes can be obtained in dependence on coverage, composition, and growth conditions [9–19]. Once formed, however, the volumetrically relaxed elastic energy of these structures largely supersedes the costs for surface and edge formation [8,20,21]. As a result, their total energy monotonically decreases as their volume increases [8,20–23], which leads to an irrevocable coarsening and Ostwald ripening as growth proceeds [24–26]. Therefore, strain-induced nanostructure formation has been universally considered to be a *nonreversible* process, meaning that a planar two-dimensional (2D) surface cannot be regained unless material is removed or strain relaxed by misfit dislocations.

In this work, we reveal that this fundamental reasoning does no longer strictly apply to nanostructures grown on vicinal surfaces. Due to the symmetry breaking induced by the deviation from the usual low-indexed surface orientations, vicinal surfaces lead to increasingly asymmetric nanostructure shapes [9,17,27–29]. In the extreme case, one-

dimensional nanowires are formed parallel [30,31] or perpendicular [32,33] to the miscut direction. These are similar to those obtained by substrate pre patterning [34,35] or anisotropic incorporation of adatoms [36,37] and present an attractive platform for realization of hole *qubits* [7,38,39] and Majorana fermions [40].

Here, we show that entropy completely alters the growth evolution and stability of Ge nanowires on vicinal Si(001) surfaces. Most unexpectedly, entropy leads to complete *reversibility* of nanowire growth, meaning that they can be completely erased and reformed by heating and cooling above, respectively, below a certain critical temperature. We follow this reversible nanomorphological transition *in vivo* using high-temperature scanning tunneling microscopy [41,42]. Most strikingly, we not only find that dissolution and reformation can be repeated many times, but even more, that the final nanostructure size and shape is solely controlled by the Ge thickness and vicinal angle independently of the growth conditions and thermal history. This reveals that the unique nanomorphologies represent equilibrium structures of the system.

Modeling the total free energy of the structures, we show that the huge step entropy of vicinal surfaces [43–45] is the key factor governing the nanomorphological transition. It renormalizes the free surface energy of the planar vicinal wetting layer, which emerges as the favored high-temperature phase in thermodynamic equilibrium, whereas the nanostructured surface is the preferred low-temperature configuration. The theoretically derived critical temperature of the phase transition scales nearly linearly with the Ge coverage—in perfect agreement with our experiments. The completely generic nature of this effect suggests that similar reversible

\*gunther.springholz@jku.at

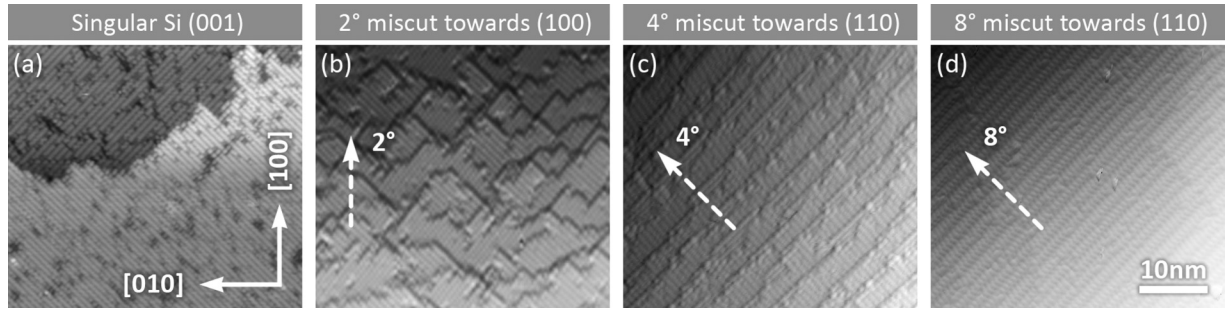


FIG. 1. STM images of the initial singular and miscut vicinal Si (001) substrate surfaces, illustrating the strong increase of the step density when the miscut angle increases from  $0^\circ$  to  $8^\circ$  from (a) to (d), respectively. The miscut direction is indicated by the dashed arrows and changes from towards (100) for panel (b), to towards (110) for panels (c), (d). The images were recorded at room temperature and the scale is the same for all.

transitions should also exist for other vicinal systems, and thus provides pathways for fabrication of perfectly controlled nanostructures for various device applications.

## II. EXPERIMENTS

Heteroepitaxial growth of Ge on vicinal Si(001) surfaces was studied for a wide range of miscut angles and growth conditions. For this purpose, a multichamber molecular-beam epitaxy and variable-temperature scanning microscopy system was employed [46–48] that allows growth and surface imaging without breaking ultrahigh vacuum conditions. After standard cleaning, the Si substrates were shortly flashed to above  $1200^\circ\text{C}$  to desorb the native oxide from the surface. Subsequently, Ge was deposited on the surface at  $1\text{ \AA}/\text{min}$  at substrate temperatures between  $450$  and  $600^\circ\text{C}$ . This was followed by various thermal heating and cooling cycles during which the surface evolution was monitored *in vivo* by reflection high-energy electron diffraction (RHEED) and variable-temperature scanning tunneling microscopy (STM). In all cases, the temperature was kept below  $600^\circ\text{C}$  to avoid Ge/Si intermixing [49–51] that would strongly alter the growth evolution. Two types of vicinal substrates were used for our investigations, namely, (i) Si (001) miscut towards the (100) direction with vicinal angles up to  $4^\circ$ , and (ii) Si miscut towards the (110) direction at angles up to  $8^\circ$  (see Fig. 1). Complementary control experiments were also performed on nominally miscut-free singular Si (001) under the same growth conditions.

In the first set of experiments, the Ge surface evolution was characterized step by step as a function of coverage after growth interruption and cool down to room temperature as described in Sec. III. In the second set, the dynamics of the surface was studied *in vivo* and real time during heating, cooling, and annealing to reveal the nanomorphological transitions and equilibrium morphologies as detailed in Sec. IV. The experimental data is analyzed and modeled in Sec. V, and in Sec. VI our equilibrium morphology model including entropy effects is presented and compared with the experiments and its consequences and implications discussed.

## III. RESULTS

Figure 1 shows the surface structure of the initial singular and vicinal Si(001) surfaces revealed by STM. The nominally

miscut-free Si surface ( $\alpha < 0.1^\circ$ ) only exhibits wide terraces that are occasionally interrupted by isolated monoatomic steps [see Fig. 1(a)]. The terraces consist of dimer rows along the  $\langle 110 \rangle$  directions, leading to the characteristic  $(2 \times 1)$  surface reconstruction. On the contrary, the vicinal surfaces [Figs. 1(b)–1(d)] display narrow trains of steps perpendicular to the miscut direction that accommodate the deviation from the exact (001) surface orientation. The distance between these steps rapidly decreases with increasing miscut angle, and their average separation is given by  $d_s = h_{\text{ML}} \cot \alpha$ , where  $h_{\text{ML}} = 1.36\text{ \AA}$  is the monolayer (ML) step height of Si(001) and  $\alpha$  the miscut angle. For the vicinal surfaces depicted in Figs. 1(b) and 1(c), the according step distances of  $3.9$ , respectively,  $1.9\text{ nm}$  are in good agreement with the STM measurements. For the very high miscut Si surface with  $8^\circ$  vicinal angle [Fig. 1(d)], due to attractive step-step interaction double layer instead of monolayer steps are formed [41,46,47].

The shape of the step edges depends on the miscut direction indicated by the dashed lines in Fig. 1. When the surface is miscut towards (110)—see Fig. 1(c), the miscut steps are aligned in the  $\bar{1}10$  direction, parallel or perpendicular to the dimer rows. Therefore, they are relatively straight and alternate from terrace to terrace between the  $S_A$  and  $S_B$  configuration [41,46,47]. For vicinal surfaces tilted towards (100) [Fig. 1(b)], the global step direction is rotated by  $45^\circ$  with respect to the Si dimers. For this reason, the steps are rather rough as they are composed of short  $S_A$  and  $S_B$  segments [48]. For Ge(001) this step faceting is, however, less pronounced [48,52]. At room temperature the steps are completely stable, but at elevated temperatures they become mobile and thus, fluctuate and meander due to thermal activation of kink formation and diffusion, as well as detachment and reattachments of adatoms [43–45]. This leads to a strong configurational disorder and increasing step entropy as the temperature increases. This affects the free energy of the system, which is the key ingredient for explaining our experiments.

For Ge/Si growth, the miscut of the vicinal surface leads to a substantial modification of the growth process. Whereas on miscut-free singular Si(001), for the given growth conditions Ge forms the well-known hut islands once a critical coverage of  $6\text{ ML}$  is exceeded (see Fig. 2), on vicinal surfaces a new growth regime emerges, in which highly faceted one-dimensional nanowirelike structures form much *before* any huts or pyramids appear. This clearly follows from the

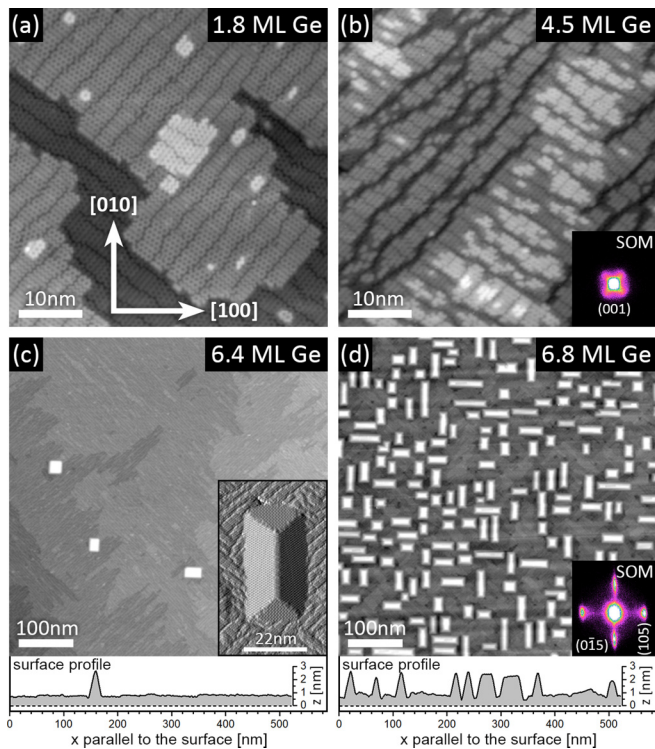


FIG. 2. STM images of Ge on miscut-free singular Si (001) recorded at Ge coverages increasing from 1.8 to 6.8 ML from (a) to (d), respectively. As shown by (c), the onset of hut island formation occurs at 6 ML. At lower coverages (a), (b), only a 2D wetting layer is formed, initially exhibiting a  $(2 \times n)$  dimer vacancy line surface reconstruction that subsequently transforms into an  $(m \times n)$  reconstruction by addition of missing dimer rows perpendicular to the vacancy lines. The hut islands exhibit a rectangular base and four equivalent  $\{105\}$  side facets [see inset in (c)], which is also seen in the surface orientation map depicted as insets in (d). The STM line profiles across the huts depicted in (c), (d) show that the huts grow on top of the wetting layer. The gray shading underneath the profiles indicates the Ge on the Si surface and the horizontal dashed line the Si/Ge interface. Ge growth was performed at 560 °C and STM images were recorded at room temperature. Note the different scales.

comparison of the STM sequences recorded for Ge growth on nominally miscut-free and on 4° miscut Si(001) presented in Figs. 2 and 3, respectively. In particular, we see that on the miscut Si surface already at 3.5 ML a perfectly faceted 1D nanoripple structure forms that seamlessly covers the whole epilayer surface—contrary to the isolated Ge huts formed on singular Si(001) [Figs. 2(c) and 2(d)]. According to Figs. 3(a) and 3(b), nanoripple formation starts via small step bunches that merge and transform into small  $(\bar{1}05)$  microfacets with patches of step-free (001) terraces in between that both rapidly expand along  $[010]$  perpendicular to the miscut direction until a fully faceted nanoripple surface is formed [Figs. 3(c) and 3(d)].

While the huts on singular Si(001) exhibit a rectangular base and four equivalent  $\{105\}$  side facets, the nanoripples seen in Figs. 3(c) and 3(d) are confined by one  $(\bar{1}05)$  side

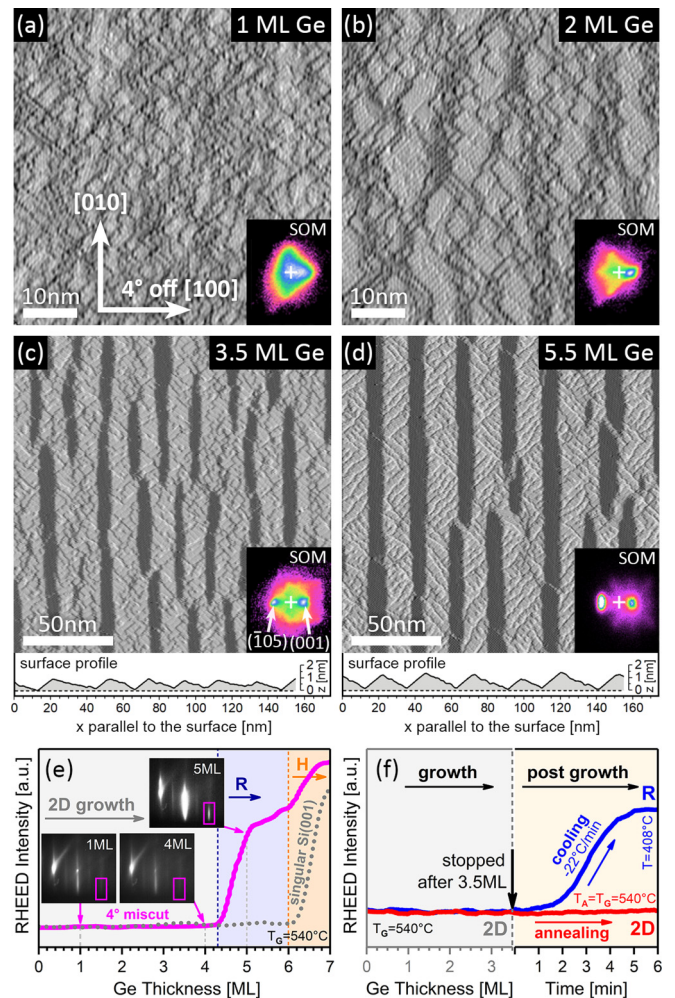


FIG. 3. Nanoripple formation for Ge growth on 4° vicinal Si (001) revealed by STM recorded at Ge coverages increasing from 1 to 5.5 ML from (a)–(d), respectively (note the different scales). The nanoripples are aligned perpendicular to the miscut direction and consist of alternating  $(\bar{1}05)$  and (001) facets as shown by the SOMs depicted as insets. Surface profiles across the ripples are depicted in (c) and (d) with the gray shading indicating the Ge and the horizontal dashed line the Si/Ge interface. Note that for better visibility of the step structure, the STM images are displayed with the gray scale corresponding to the local derivative of the height in the horizontal direction. The STM images were recorded after Ge growth at  $T_G = 540$  °C and cooling to room temperature. In (e) the RHEED intensity evolution during growth is shown, indicating a critical coverage of 4.3 ML for the onset of ripple formation (solid line). Also plotted is the intensity evolution for Ge on zero miscut singular Si (001) (dotted line), where the onset of hut island formation occurs much later at a critical coverage of 6 ML (see Fig. 2). The insets show the RHEED patterns at different stages of growth and the rectangles the region where the intensity evolution was recorded. Panel (f) displays the RHEED intensity evolution *after* growth was stopped at 3.5 ML. In one case, the temperature was kept constant at 540 °C (red trace); in the other case, the temperature was ramped down by  $-22$  °C/min to room temperature (blue trace). No intensity change occurs during annealing but only during cooling. This signifies that the nanoripples observed by STM at 3.5 ML are actually formed not during but *after* growth during the cooldown process.

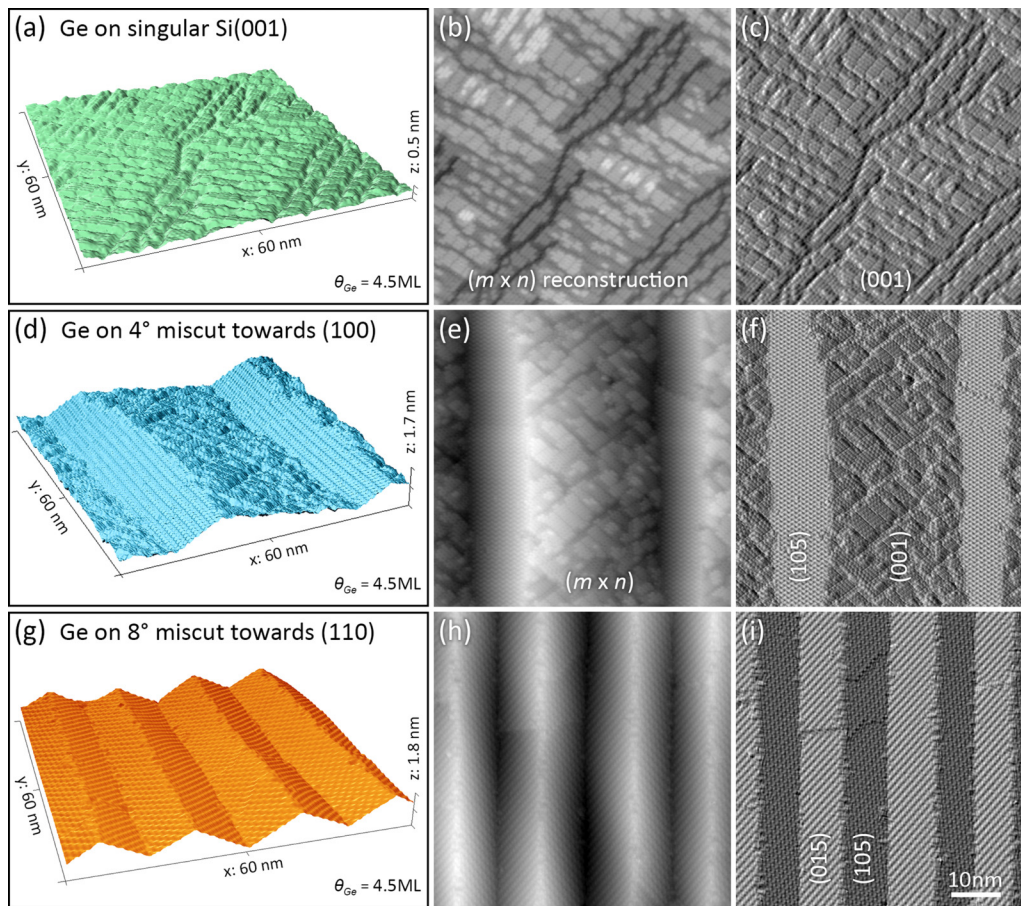


FIG. 4. High-resolution STM images of the Ge surface at 4.5-ML coverage on zero miscut (top row),  $4^\circ$  miscut (middle row), and  $8^\circ$  miscut vicinal Si(001) substrates (bottom row), evidencing the completely different surface topography formed at the same Ge thickness. On singular Si(001) a flat 2D Ge wetting layer with  $(m \times n)$  reconstruction forms, whereas the miscut surfaces are completely covered by 1D nanoripples. For the  $4^\circ$  vicinal surface the ripples are asymmetric with alternating (105) and (001) side facets, whereas for the  $8^\circ$  miscut surface they are symmetric with equal (105)/(015) side facets. Note that the miscut direction is different in the two cases. The (105) facets exhibit the horseshoe reconstruction described in Ref. [54], whereas the (001) ripple facets exhibit the same  $(m \times n)$  reconstruction as seen for the 2D Ge wetting layer on singular Si (001). The STM images are displayed in 3D representation, grayscale topography as well as derivative mode, from left to right, respectively, and the lateral scale is the same for all images.

facet on the right and one (001) facet on the left, whereas the other three {105} hut facets are missing. This is proven by the surface orientation maps (SOMs) [9,14,53] depicted as insets in the STM images of Figs. 2 and 3, which for the 1D nanoripples feature only two intensity maxima at the  $(\bar{1}05)$  and (001) orientations (see arrows), whereas for the huts four symmetric {105} peaks appear. Moreover, whereas for the hut-covered Si(001) surface the central SOM (001) maximum from the 2D wetting layer is still present after hut formation, for the rippled surface this central maximum completely disappears (crosses in SOM insets in Fig. 3). This signifies that the hut islands grow on top of an intact wetting layer, whereas on the  $4^\circ$  miscut surface it is totally consumed by nanoripple formation. This is also demonstrated by the STM surface profiles shown in Figs. 2 and 3, respectively, evidencing that the 2D wetting layer is still present between the huts, whereas the ripples excavate the wetting layer until their base reaches the Si/Ge interface.

The drastic difference in the growth morphology on singular and vicinal Si (001) is illustrated by Fig. 4, which shows

the Ge surface structure at the same 4.5-ML coverage on the different surface orientations at high resolution. On singular Si(001), the 2D Ge surface is flat and only displays the characteristic  $(m \times n)$  surface reconstruction [Figs. 4(a)–4(c)] arising from the formation of dimer vacancy lines and missing dimer rows (see Ref. [41] and references therein). For the 1D rippled surface on  $4^\circ$  vicinal Si(001), the same  $(m \times n)$  reconstruction appears on the (001) ripple facets [see Figs. 4(d)–4(e)], whereas the opposing  $(\bar{1}05)$  ripple facets are practically step-free and exhibit the characteristic horseshoe reconstruction [54]. Also shown in Figs. 4(g)–4(i) are nanoripples formed on the  $8^\circ$  miscut Si (001) surface where the miscut direction is towards (110). Evidently, a perfectly faceted nanoripple structure is formed as well; however, the ripples are now symmetric with equal {105} facets on both sides.

To determine the exact onset of 1D nanoripple formation we have measured the intensity evolution of various RHEED diffraction spots *in situ* during growth. The result is displayed in Fig. 3(e), evidencing that during Ge growth on  $4^\circ$  miscut Si(001) at  $540^\circ\text{C}$  the onset occurs at 4.3 ML

where a strong change in diffracted intensity occurs. This is in striking opposition to what is seen by STM after cooling to room temperature, where ripples are observed already much earlier at 3.5 ML [Fig. 3(c)]. To shed light on this surprising contradiction, we tracked the RHEED intensity evolution after the end of growth, considering two cases, namely, (i) that the temperature is kept constant after 3.5-ML Ge growth, and (ii) that the sample is slowly cooled down immediately after growth by  $-22$  °C/min to room temperature as done for the STM measurements. The results are summarized in Fig. 3(f) by the red and blue lines, respectively, evidencing that when the temperature is kept constant, the diffracted intensity remains fixed and does not show any changes even for hours of further annealing. This reveals that the 2D surface remains flat and is stable without any signs of nanoripple formation. On the contrary, when the sample temperature is ramped down [red trace in Fig. 3(f)], the diffracted intensity strongly increases once the temperature falls below 500 °C. This signifies that at this coverage the nanoripples observed at room temperature are actually not formed during but *after* growth during the cooldown process! This completely unexpected phenomenon contradicts the common notion that the STM images recorded at room temperature perfectly represent the actual morphology formed during growth. This suggests a remarkably large amount of mass transport occurring at moderate temperatures even after growth has been completed.

#### IV. REVERSIBLE NANORIPPLE FORMATION

To shed light on this unexpected behavior, we employed *in vivo* high-temperature STM to clarify how the surface evolves as a function of temperature during heating and cooling. The result for Ge on 4° miscut Si(001) is shown in Fig. 5, where in the sequence of STM images we start in (a) with the well-developed nanoripples formed after 4.6-ML Ge deposition and cooldown to room temperature, similar as shown in Fig. 3. Subsequently, we ramped the temperature slowly up in steps to 580 °C and then back to room temperature while STM images were continuously recorded. Snapshots from these STM movies are shown in Figs. 5(b)–5(f), with their color indicating the temperature at which the images were recorded (see color scale on the right-hand side). Starting from perfectly faceted initial nanoripples, heating to 500 °C evidently does not have any noticeable effect on the ripple structure [see Fig. 5(b)]. Above 500 °C, however, the ripples start to dissolve [Fig. 5(c)] such that at 580 °C a completely flat 2D surface is regained [see Fig. 5(d)]. Conversely, when we subsequently lower the temperature slowly down again, the ripples gradually reappear such that below 500 °C the fully faceted ripple structure is restored.

Remarkably, we can repeat this dissolution and reformation process many times without any appreciable change in the final ripple structure. This is evidenced by the STM image displayed in Fig. 5(f) that displays the ripple surface formed after *five* consecutive annealing/cooling cycles. Evidently, the such-obtained ripple structure is indiscernible from that directly after growth [Fig. 5(a)]. Thus, ripple formation is not only *fully reversible*, but even more, the final structure turns out to be completely independent of the thermal history of the samples and initial growth conditions. This suggests that

the ripples represent a unique equilibrium morphology that is completely stable and below a critical temperature, whereas above this temperature the 2D surface is the thermodynamic equilibrium configuration of the system. This is the key result of our work.

To determine how the critical transition temperature depends on the Ge coverage, we have performed an extended series of annealing experiments for Ge coverages varying between 3 and 5 ML. In this case, we have used *in situ* RHEED to track the surface evolution as a function of temperature as summarized in Fig. 5(g). Evidently, for all coverages a fully reversible 3D/2D transition occurs, characterized by a crossover from a high diffraction intensity for the nanoripple phase to a low-intensity for the 2D phase when the sample is heated and its reversal when cooling back to the starting temperature. It is noted that for each coverage completely identical traces are observed during repeated annealing cycles, which are plotted in Fig. 5(g) on top of each other. This underlines the perfect reversibility and reproducibility of the 2D to ripple transition and confirms its thermodynamic origin.

Most importantly, we find that the transition shifts to higher temperatures as the Ge coverage increases. For 3-ML Ge, it occurs at around 465 °C, whereas it shifts to 570 °C at 5 ML. Also, a hysteresis between heating and cooling is seen for all cycles, as is typical for first-order phase transitions. The hysteresis is found to depend on the heating/cooling rate and narrows down to a few degrees when the rates are reduced to  $\pm 1$  °C/min. Therefore, it is attributed to kinetic effects. This explains why the hysteresis is wider at lower Ge coverages because in this case the transition occurs at lower temperatures where surface diffusion is reduced. Because we do not observe any change in the transition temperature and final ripple shape after many annealing cycles, Si/Ge intermixing or interdiffusion is negligible under the given conditions [46], as this would clearly change the behavior of the system.

The complete dataset allows us to construct a comprehensive equilibrium phase diagram of Ge on the vicinal Si surface presented in Fig. 5(h) that depicts the equilibrium morphologies formed as a function of temperature and Ge thickness. Clearly, for coverages up to 5.5 ML, the surface is either in the ripple phase (blue region) or in the 2D phase (gray region), and the chosen configuration only depends on the coverage and temperature. The black data points mark the critical transition temperatures (midpoints of the hysteresis curves) derived from our annealing experiments and the blue triangles the critical coverages for the ripple onset detected during growth. Evidently, the results agree well with each other. The black solid line separating the two phases represents the critical transition temperature  $T_C$  as a function of coverage derived from our total free-energy model described in Sec. VI, which predicts that the critical temperature rises almost linearly with the Ge coverage as seen in our experiments. Also indicated in the phase diagram is the onset of hut nucleation on top of the ripples (red diamonds), which occurs at about 5.8 ML more or less independently of temperature, as well as the regime above 600° where higher aspect ratio pyramids and domes are formed (red shaded region). At these temperatures, Si/Ge intermixing sets in [12,49–51] and thus, the full reversibility of the nanomorphological transition is lost, meaning that the dome islands do not dissolve during

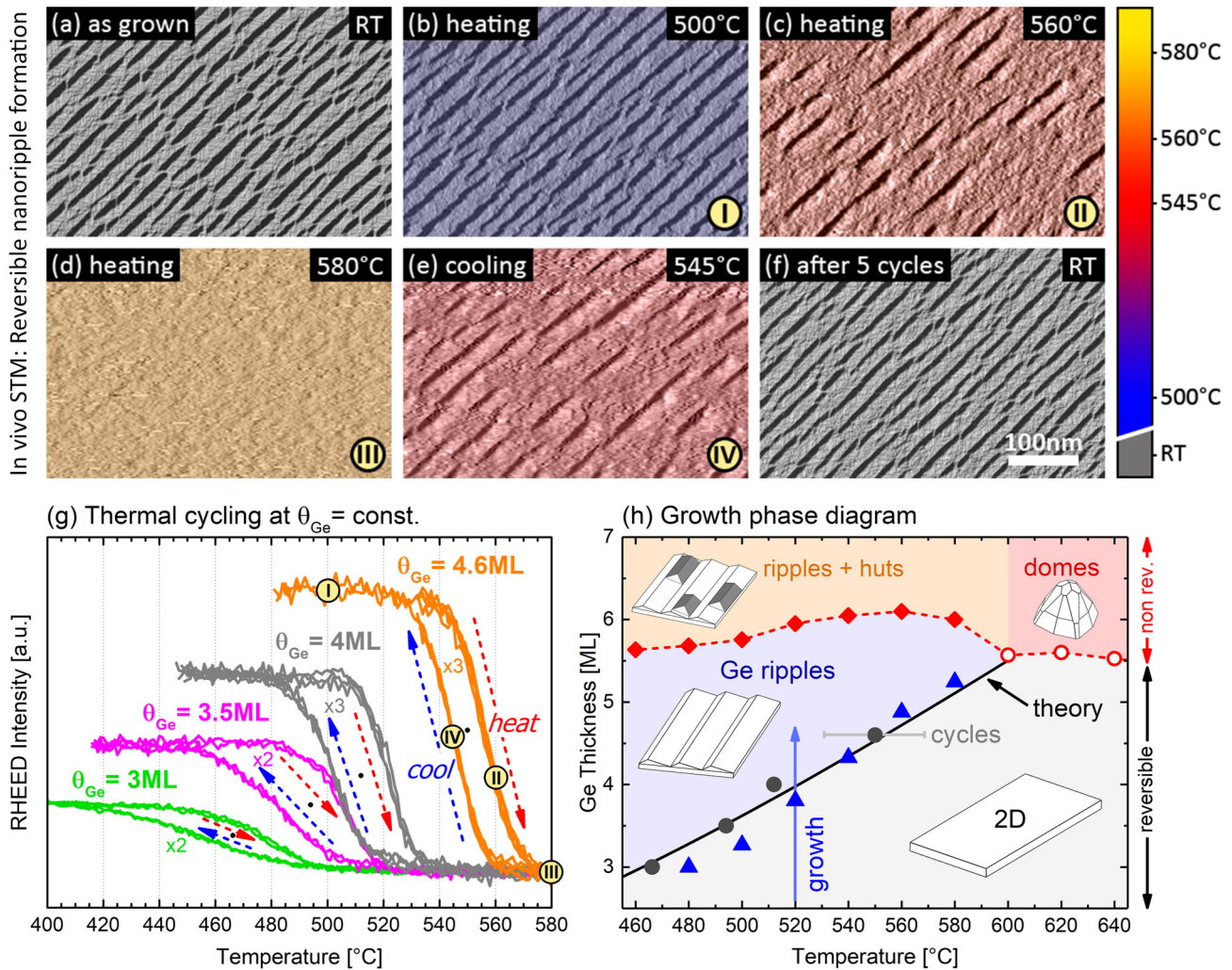


FIG. 5. Fully reversible Ge nanoripple formation on  $4^\circ$  vicinal Si (001) with miscut towards (100) revealed by *in vivo* high-temperature STM and RHEED. The sequence of STM images in (a)–(f) was recorded during heating of 4.6-ML Ge from room temperature to 500, 560, and 580 °C, and then cooling back to 545°C and finally room temperature. Complete ripple dissolution takes place at 580 °C and the ripples reform when the temperature is lowered back to below 520 °C. No difference between the initial and final ripple structure is seen after five complete annealing cycles (f). Panel (g) displays RHEED intensity curves recorded as a function of temperature during multiple heating/cooling cycles ( $r_T = \pm 12$  °C/min) for fixed Ge coverages between 3 and 4.6 ML. The yellow labels on the orange curves denoted by roman numerals correspond to the STM images shown in (b) to (e), respectively. Evidently, the transition temperature increases with Ge thickness. For each coverage, several heating/cooling cycles ( $\times 2$  and  $\times 3$ ) are plotted on top of each other. The resulting equilibrium surface phase diagram is shown in (h). Black dots represent the 2D/3D transition temperature from the annealing experiments and the blue triangles the ripple onset during growth [cf. Fig. 3(e)]. The black solid line represents the critical transition temperature derived by total free-energy calculations [Eq. (8)]. Red diamonds indicate the transition from ripples to huts, and the red circles the formation of multifaceted domes at higher temperature and higher coverages. STM images are displayed in derivative mode with a coloring indicating the temperature at which the images were recorded (see scale on the right).

annealing but only coarsen, just as has been observed on miscut-free singular Si(001) [55–58]. Although between the isolated pyramids and domes, 1D nanoripples appear during the cooldown process, these ripples do not attain the same size and uniformity of those of initial samples because the wetting layer is depleted by the material incorporated in the domes and pyramids. This is described in more detail in the Supplemental Material [59].

The reversible nanoripple formation is not unique for a particular vicinal surface but occurs for a wide range of miscut angles and directions. This is proven by analogous

experiments performed for other vicinal Si(001) surfaces, in which similar 1D nanoripples form, albeit with different ripple geometries and facet angles as illustrated by Fig. 4. In particular, we find in all cases that the low-temperature nanoripple structures dissolve when heated above a certain critical temperature and that it reforms when the sample is cooled back below. This is demonstrated by Fig. 6 for Ge ripples formed on  $8^\circ$  vicinal Si(001), where a similar sequence of *in vivo* STM images recorded during annealing and cooling is depicted. Evidently, ripple dissolution/reformation occurs at a similar temperature as on the  $4^\circ$  vicinal Si surface (Fig. 5),

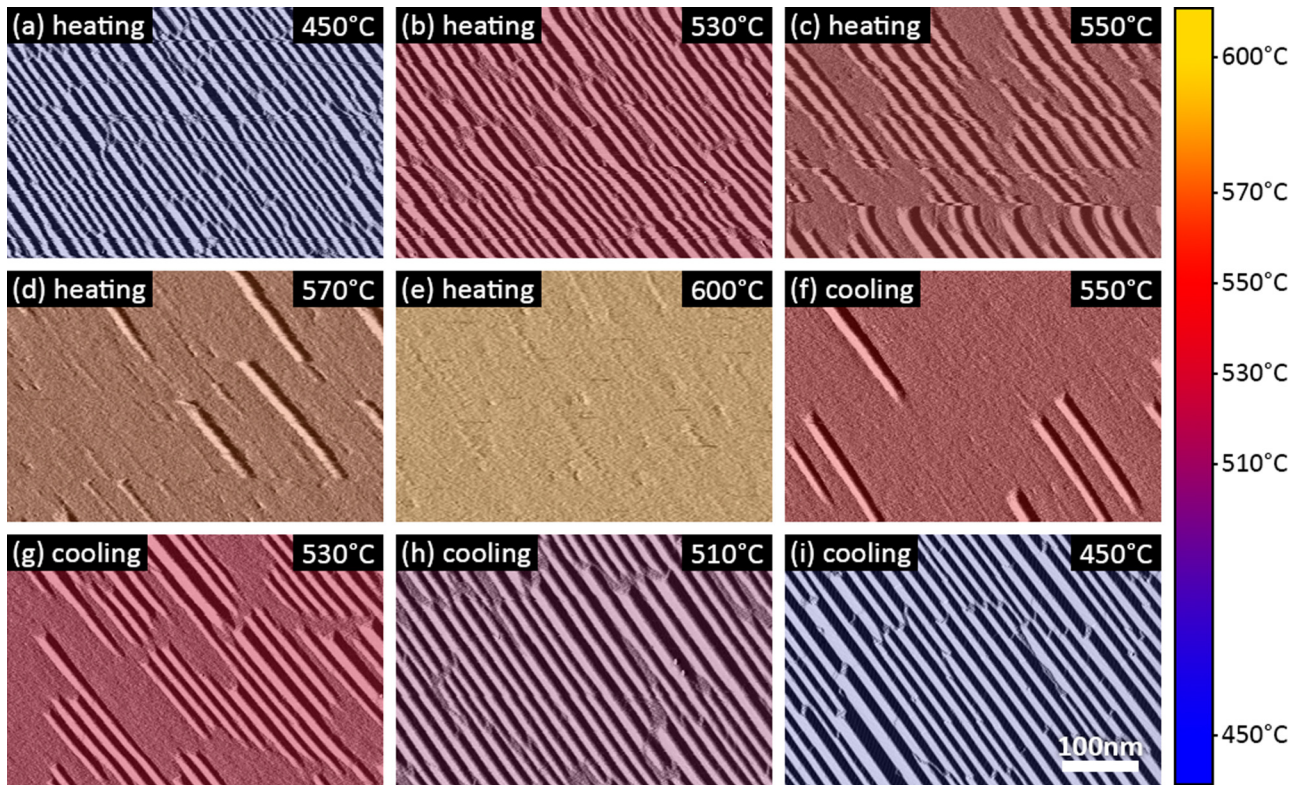


FIG. 6. Fully reversible Ge nanoripple formation on 8° vicinal Si(001) with miscut towards (110), as seen by *in vivo* high-temperature STM. The STM images were recorded during heating and cooling, where the temperature was first ramped from 450 to 600 °C (a)–(e) and then back to 450 °C (g)–(i) as indicated. The Ge coverage was fixed at 4.7 ML. The STM images are displayed in derivative mode with their color indicating the temperature at which the images were recorded (see scale bar on the right-hand side).

which is remarkable because the ripples on 8° miscut Si exhibit a different ripple geometry defined by two symmetric {105} ripple facets on both sides (see Fig. 4), whereas the ripples on the surfaces miscut towards (100) are asymmetric and terminated by only one (105) and one (001) side facet. Even more, we observe a similar monotonic increase of the critical phase transition temperature from 460 to 560 °C as the Ge coverage increases, closely resembling the behavior of the other ripple surfaces [Fig. 5(h)]. This highlights the completely universal nature of the reversible ripple formation process and its thermodynamic origin that is deterministically controlled solely by the Ge coverage and temperature.

## V. SCALING OF THE NANORIPPLE PERIOD

A very appealing feature of the 1D nanostructures is the almost deterministic control of size and period by tuning the Ge coverage, independently of the growth and annealing conditions. This arises from the fact that ripple formation is a self-limited process that stops once the wetting layer is consumed and the Si/Ge interface is reached. Because the ripples seamlessly cover the whole epilayer surface, the ripple volume then exactly equals the amount of Ge deposited, and due to the triangular ripple cross section, the ripple height  $h_R$  is simply twice the deposited Ge thickness. As a result, the equilibrium ripple period  $p_R$  and width is expected to scale linearly with the Ge coverage  $\theta_{Ge}$  as

$$p_R = \lambda_\alpha \theta_{Ge}, \quad (1)$$

where the scaling factor  $\lambda_\alpha$  only depends on the aspect ratio and geometry of the ripples.

To verify this prediction, we have analyzed the equilibrium ripple periods for a wide range of coverages and miscut angles using Fourier transformation (FT) and autocorrelation (AC) analysis, exemplified by Fig. 7 for 4.5-ML Ge on 2°, 4°, and 8° vicinal Si(001). The left-hand side of this figure shows the STM images recorded after slow cooling through the 2D/1D ripple transition, together with the cross sections of the FT power spectrum that feature sharp peaks due to the good ordering of the nanoripples in the lateral direction. From the FT peak distance the average ripple period was derived as  $p_R = 38.3, 28.8,$  and  $16.4$  nm for  $\alpha = 2^\circ, 4^\circ,$  and  $8^\circ$ , respectively. This factor of 2.5 change is solely caused by the difference in ripple geometry and agrees very well with the autocorrelation function cross-section analysis shown in Fig. 7(e), where the average ripple spacing is derived from the position of the first AC maximum indicated by the arrows. In each case, the values obtained by the different methods agree well with each other.

In Fig. 8, the experimentally measured ripple periods are plotted for each miscut angle as a function of Ge coverage. The results demonstrate a perfect linear scaling as predicted by Eq. (1) represented by the dashed lines. As the ripple geometry changes as a function of the miscut angle and direction, the scaling parameter  $\lambda_\alpha$ , i.e., slope of the dashed lines differs for each miscut angle. If we define the ripple geometry in terms of the inclination angles  $\alpha$  and  $\beta$  of the

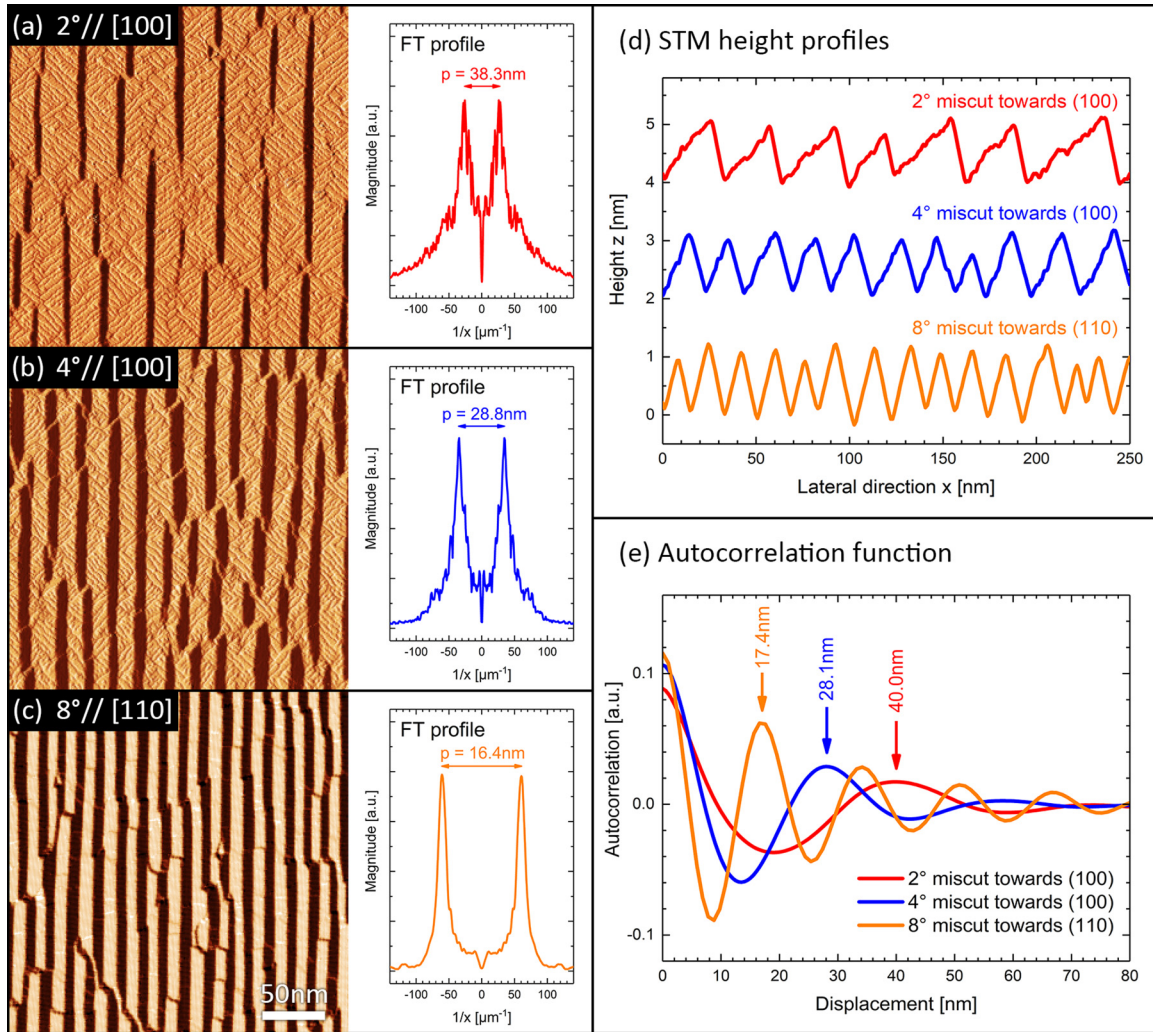


FIG. 7. Ge nanoripple period at 4.5 ML coverage on 2°, 4°, and 8° vicinal Si(001) surfaces determined by Fourier transform and autocorrelation analysis of corresponding STM images shown in (a)–(c), respectively. Line profiles through the FT power spectrum (middle column) exhibit sharp peaks and their distance corresponds to the inverse ripple period  $p$ . STM line profiles across the ripples and horizontal autocorrelation function profiles are shown in (d) and (e), respectively. For the latter, the average ripple period is given by the position of the first AC peak as indicated by the arrows.

ripple facets with respect to the original vicinal surface [see inset in Fig. 8(b)], the scaling parameter can be easily derived as

$$\lambda_{\alpha} = 2h_{\text{ML}}(\cot \alpha + \cot \beta), \quad (2)$$

where  $h_{\text{ML}} = a_0/4$  is the height of one monolayer on the surface. For the ripples on vicinal surfaces miscut towards (100) confined by alternating (001) and (105) facets,  $\alpha$  is simply the miscut angle away from (001) and  $\beta = (11.3^\circ - \alpha)$ , where  $11.3^\circ$  is the angle between (105) and (001) facets at the top of the ripples. The resulting dependence of  $\lambda_{\alpha}$  versus miscut angle is shown in Fig. 8(b), indicating that with increasing  $\alpha$ ,  $\lambda_{\alpha}$  first rapidly decreases but then saturates at a minimal value of  $\lambda_{\alpha} = 5.6 \text{ nm/ML}$  at  $\alpha = 5.65^\circ$ , where the ripples become symmetric ( $\alpha = \beta$ ) and thus exhibit the highest aspect ratio. For larger miscut angles, the ripple asymmetry and accordingly,  $\lambda_{\alpha}$  again increases. The experimental scaling values (full circles) obtained from the fits of the data in (a) nicely fall

on the theoretical line, evidencing that our model assumptions hold.

For the nanoripples formed on the vicinal surface with 8° miscut towards (110) [Figs. 4(g)–4(i) and 5], the two {105} ripple facets are symmetric and inclined by  $\alpha = \beta = 7.97^\circ$  to the vicinal substrate surface. This yields a scaling parameter of  $\lambda_{\alpha} = 4 \text{ nm/ML}$  represented by the orange dashed line in Fig. 8(a), which is again in perfect agreement with our experimental data. Thus, our model applies for a wide range of surface orientations. It is noted that Si/Ge intermixing and the existence of a nonzero wetting layer underneath the ripples would significantly affect the scaling behavior [Eq. (1)]. Intermixing would increase the ripple size because there would be more material available for ripple formation. The opposite occurs if part of the Ge is absorbed in a nonzero 2D wetting layer. As detailed in the Appendix the former would increase the slope and scaling parameter  $\lambda_{\alpha}$ , whereas the latter would rigidly shift the linear dependence to higher coverages. Both alterations are not compatible with our experimental data and

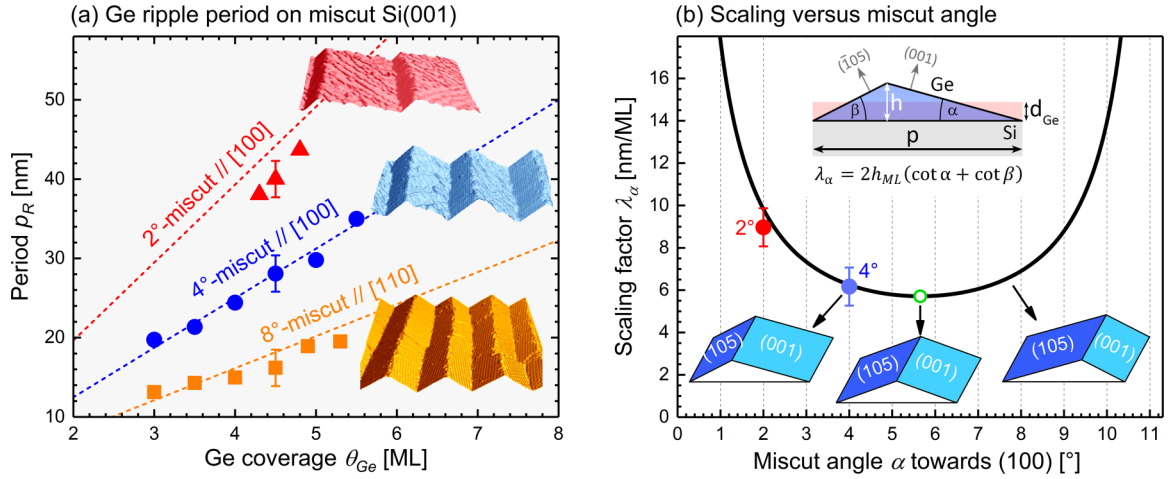


FIG. 8. Scaling of the equilibrium ripple period  $p_R$  as a function of Ge coverage for three different vicinal Si surfaces. The red triangles and blue dots correspond to the vicinal surfaces with 2° and 4° miscut towards (100), the orange squares to those on 8° miscut Si tilted towards (110). Data points were derived by analysis of STM images recorded after slow cooling through the 2D/3D transition (see Fig. 7). The dashed lines represent the ripple period predicted by Eq. (1) using the scaling parameter  $\lambda_\alpha$  of Eq. (2). High-resolution STM images are shown as insets. Panel (b) shows how  $\lambda_\alpha$  varies as a function of miscal angle  $\alpha$  tilted towards (100). The symbols represent the experimental values obtained from the fit of the data.

can be ruled out on the basis of our experiments (see Fig. 10 in the Appendix).

## VI. THE CRITICAL PHASE TRANSITION TEMPERATURE

To clarify the origin on the reversible ripple formation, we consider the free-energy difference between the ripples and the 2D surface. For strained heteroepitaxial systems, this difference comprises several contributions [30,60] that can be summarized by

$$\Delta E_{\text{tot}} = E_R - E_{2D} = \Delta E_{\text{strain}} + \Delta E_{\text{surf}} + \Delta E_{\text{edge}}. \quad (3)$$

In this relation,  $\Delta E_{\text{strain}} (<0)$  is the elastic energy relaxed by ripples relative to strain energy of the fully pseudomorphic 2D wetting layer, obtained, e.g., by solution of the equilibrium stress equations as shown in Fig. 9(a).  $\Delta E_{\text{surf}}$  is the free surface energy difference between the ripples and the 2D surface, and  $\Delta E_{\text{edge}}$  the energy associated with the additional edges formed between the ripple facets. When  $\Delta E_{\text{tot}} < 0$ , the ripple phase is favored, whereas for  $\Delta E_{\text{tot}} > 0$ , the 2D surface is the stable configuration. The relaxed elastic energy per unit ripple volume  $\rho_{el}$  is fixed for a given ripple geometry [30,60], and because in our case the ripple volume is equal to the volume of the wetting layer,  $\Delta E_{\text{strain}}$  scales linearly with the Ge coverage. On the contrary,  $\Delta E_{\text{surf}}$  is practically constant because the ripples seamlessly cover the whole epilayer surface and thus, the overall exposed facet areas do not change with the Ge coverage—not considering any changes of surface energies as a function of distance from the interface that can be only obtained by density-functional theory calculations [61–63]. Last but not least, because the ripple width scales linearly with the coverage [Fig. 8(a)] and there are exactly two edges per ripple,  $\Delta E_{\text{edge}}$  scales inversely to the Ge coverage. All in all, per unit area, the total energy difference thus

reads as

$$\Delta E_{\text{tot}}/A = -\rho_{el}h_{ML}\theta_{Ge} + \gamma_R^* - \gamma_{2D} + \frac{e_{\text{edge}}}{\lambda_\alpha\theta_{Ge}}, \quad (4)$$

where  $\gamma_R^* = 2h_0(\gamma_{001}\csc\alpha + \gamma_{105}\csc\beta)/\lambda_\alpha$  is the projected surface energy of the (001) and (105) ripple facets,  $\gamma_{2D}$  the surface energy of the vicinal wetting layer, and  $e_{\text{edge}}$  the edge energy per unit ripple length.

At sufficiently large coverages, the energy difference is dominated by the first term of Eq. (4), i.e., the volumetric energy relaxation. This means that beyond a certain critical coverage  $\theta_c$ , the 3D ripple phase will be always favored over the 2D phase, independently of the growth conditions and temperature. To explain the reversibility of the ripple transition, we thus need to look at the temperature dependence of the factors entering in Eq. (4) and take them into account. If we consider a fixed ripple shape and composition, the relaxed elastic energy density  $\rho_{el}$  is temperature independent—not considering the minute changes in lattice parameters and elastic constants that are too small to have any noticeable effect. The edge energies are also unlikely to change significantly as long as the atomic configuration at the facet edges remains unchanged. This leaves surface energies as main sources for the free-energy renormalization. Specifically, because the reversibility of the nanoripple formation is linked to the vicinity of the substrate surface, we suggest that the large step entropy of the densely stepped wetting-layer surface is the key source for this renormalization process.

At elevated temperatures, surface steps start to meander and fluctuate via thermal kink formation and annihilation [43–45,52,64–66]. The resulting increase in configurational disorder reduces the free surface energy of the vicinal wetting layer according to

$$\gamma_{2D,\alpha}(T) = \gamma_{2D,0} - n_{s,\alpha}T S_s, \quad (5)$$

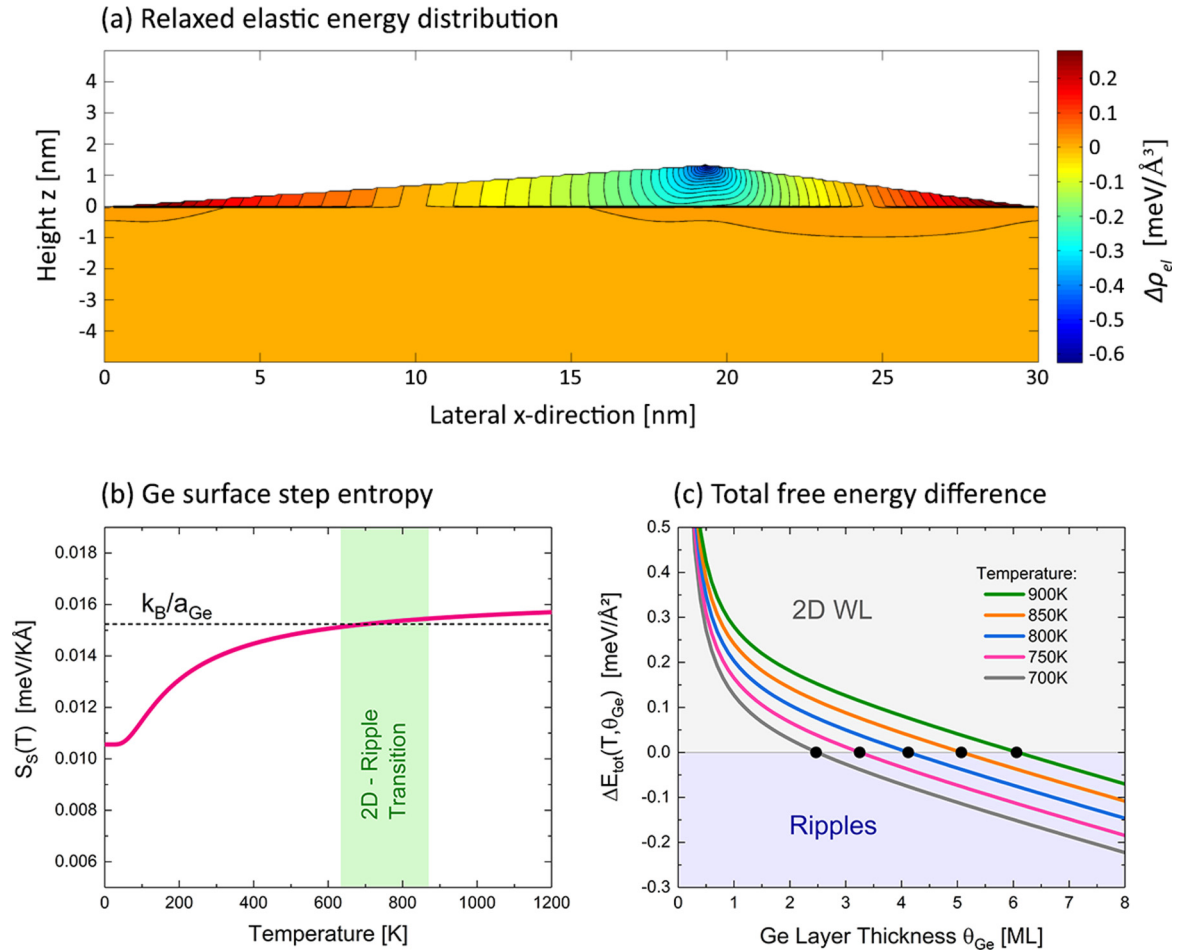


FIG. 9. Energetics of nanoripple formation for Ge on  $4^\circ$  miscut Si (001). (a) Relaxed elastic energy distribution  $\Delta\rho_{el} = (\rho_R - \rho_0)$  relative to the strain energy density  $\rho_0$  without relaxation derived by solution of the surface stress equation in the shallow slope approximation [64,65], giving an average value of  $0.024 \text{ meV}/\text{\AA}^3$ . (b) Temperature dependence of the Ge step entropy given by Eq. (6) for Ge miscut steps along [010] based on Ref. [52]. The green shaded region indicates the temperature range pertaining to our experiments, in which the step entropy can be approximated by  $S_s^* \cong k_B/a_0$  as indicated by the horizontal dashed line. (c) Total energy difference  $\Delta E_{\text{tot}} = E_R - E_{2D}$  per unit area between the ripples and the vicinal 2D wetting layer including step entropy plotted as a function of Ge coverage for different temperatures between 700 and 900 K. For  $\Delta E_{\text{tot}} > 0$  the flat vicinal 2D surface is favored; for  $\Delta E_{\text{tot}} < 0$  the ripples are the lower energy configuration. The zero values of  $\Delta E_{\text{tot}} = 0$  (black dots) correspond to the phase boundary shown as black solid line in Fig. 5(h).

where  $S_s$  is the step entropy,  $n_{s,\alpha}$  the step density of the vicinal surface, and  $\gamma_{2D,0}$  the surface energy at zero Kelvin without entropy corrections. Obviously, the magnitude of the entropy contribution [second term in Eq. (5)] is proportional to step density and thus, particularly large for high miscut vicinal surfaces ( $n_{s,\alpha} \sim \tan \alpha$ ). As a result, the surface energy of the vicinal wetting layer substantially decreases when the temperature increases—in contrast to the low-indexed, practically step-free ripple facets (see Fig. 4) where this effect can be neglected. The surface energy of the ripples  $\gamma_R$  can thus be assumed to be temperature independent, i.e., the step entropy only reduces the free energy of the vicinal wetting layer, shifting the total free-energy balance towards the 2D phase once a critical temperature is reached.

For Ge (001), step meandering becomes significant above the so-called freeze-in temperature  $T_F = 575 \text{ K}$  [52], which well applies for our experimental conditions. The step entropy of [010] Ge surface steps consists of the sum of step meandering  $S_m$  and vibrational entropy  $S_{\text{vib}}$  and has been derived by

Zandvliet [52] as

$$S_s = S_m + S_{\text{vib}} = \frac{k_B}{a_0} \ln(1 + e^{-\delta/2k_B T}) - \frac{3k_B}{2a_0} \ln\left(\frac{1 - e^{-\Theta_S/T}}{1 - e^{-\Theta_T/T}}\right). \quad (6)$$

In this equation,  $\delta = -5 \text{ meV}$  is the next-nearest atom interaction energy at the surface steps, which for Ge (001) is very small [52], meaning that  $S_m$  is practically constant above 500 K. The vibrational entropy (second term) arising from the reduced coordination of the step atoms is determined by the Debye temperatures  $\Theta_S = 264 \text{ K}$  and  $\Theta_T = 341 \text{ K}$ , respectively [52], and is thus also only very weakly temperature dependent. The sum of both is plotted as a function of temperature in Fig. 9(b), indicating that the step entropy can be approximated as  $S_s^* \cong k_B/a_0$  in the temperature range pertaining to our experiments [shaded region in Fig. 9(b)]. It is to be noted that Eq. (6) does not include step-step interactions or possible step faceting [52], which however would

not change the generic behavior of the free surface energy renormalization. Combining all terms, the total free-energy difference per unit area with step entropy included now reads as

$$\Delta E_{\text{tot}}(T, \theta_{\text{Ge}})/A \cong -\rho_{\text{el}} h_{\text{ML}} \theta_{\text{Ge}} + \Delta\gamma_{s,0} + n_{s,\alpha} S_s T + \frac{e_{\text{edge}}}{\lambda_0} \frac{1}{\theta_{\text{Ge}}}, \quad (7)$$

where  $\Delta\gamma_{s,0} = \gamma_{R,0}^* - \gamma_{2D,0}$  denotes the surface energy difference without entropy corrections. For the  $4^\circ$  miscut case, the corresponding dependence of  $\Delta E_{\text{tot}}$  as a function of Ge coverage is shown in Fig. 9(c) for different temperatures between 700 and 900 K, demonstrating that the critical coverage (black dots) below which the ripples are the lower free-energy configuration increases when the temperature increases.

At the 2D-3D phase transition, the free energy of the ripples and the 2D wetting layer must be equal, i.e.,  $\Delta E_{\text{tot}} = 0$ . Inserted in Eq. (7), this yields the critical transition temperature  $T_c$  as

$$T_c(\alpha, \theta_{\text{Ge}}) = \frac{1}{n_{s,\alpha} S_s} \left( -\Delta\gamma_{s,0} + \rho_{\text{el}} h_{\text{ML}} \theta_{\text{Ge}} - \frac{e_{\text{edge}}}{\lambda_\alpha} \theta_{\text{Ge}}^{-1} \right) \quad (8)$$

that is to be compared to our experiments. For the  $4^\circ$  miscut Si(001) surface, the step density is  $n_s = 0.05 \text{ \AA}^{-1}$  and the elastic energy relaxation per unit volume  $\rho_{\text{el}} = 0.024 \text{ meV/\AA}^3$  obtained by solving the surface-stress equations in the shallow slope approximation [67,68] [see Fig. 9(a)]. Using  $S_s^* \cong k_B/a_0$  from Fig. 9(b) and  $e_{\text{edge}} = 8 \text{ meV/\AA}$  as suggested by Retford *et al.* [69], the slope  $\partial T_c / \partial \theta_{\text{Ge}}$  is in perfect agreement with the experiments without adjustable parameters, as demonstrated by the solid black line in Fig. 5(h). Moreover, from the fit of the absolute  $T_c$  values of our experiments, the zero Kelvin surface energy difference between the ripple and 2D phase is obtained as  $\Delta\gamma_{s,0} = -0.5 \text{ meV/\AA}^2$ . Thus, the reversible nanomorphological transition as well as its scaling with Ge thickness is nicely explained. It is further noted that the existence of the reversible 2D/3D transition does not rely on particular details of the step structure of the vicinal surface, as the step entropy will always reduce the free surface energy of the vicinal surface when the temperature increases, whereas the perfect nanofacets of the 3D structure are little affected. This is the fundamental basis for the reversible transition and the reason why this transition occurs for such a wide range of vicinal surfaces and varying ripple geometries investigated in our work.

According to Eq. (8), the critical temperature  $T_c \sim 1/n_{s,\alpha} S_s$  scales inversely to the step density on the wetting layer. This means that  $T_c$  is sufficiently low only for high miscut surfaces and explains why a similar reversible transition does not occur on step-free Si(001) where the effect of step entropy is very small. It is to be noted, however, that with changing miscut angle not only the step density  $n_s$ , but also the ripple shape and thus, the surface energy difference  $\Delta\gamma_{s,0}$  as well as elastic energy relaxation  $\rho_{\text{el}}$  change. These changes, however, tend to cancel each other in Eq. (8), for which reason the  $T_c$ 's in our experiments occur in a similar temperature range for a wide range of miscut angles.

Our model also explains why the reversibility is lost once higher aspect ratio structures such as pyramids or domes

are formed on the surface, because in this case, the elastic energy relaxation  $\rho_{\text{el}}$  drastically increases, which shifts  $T_c$  upwards into the regime where irreversible coarsening [56,70] and Si/Ge intermixing sets in [12,49–51]. This completely alters the energetic and thus, the morphological evolution of the system. Most importantly, our model [Eq. (8)] predicts that the critical temperature  $T_c$  scales nearly linearly with the Ge thickness—in perfect agreement with our experiments. This, together with the perfect tunability of the ripple period distinguishes the ripple formation process of strained epilayers from faceting and defaceting transitions of vicinal bulk crystal surfaces [71–73], in which case the transition occurs at significantly higher temperatures and the facet and ripple sizes continuously coarsen and grow in time [70–72], which does not occur in our experiments.

## VII. CONCLUSION

Entropy effects substantially modify the growth and stability of self-assembled epitaxial nanostructures formed on vicinal surfaces. For the Ge/Si system this unexpectedly leads to a full reversibility of nanostructure formation, meaning that these can be reproducibly erased and reformed many times, returning to a final structure that is completely independent of the growth conditions and thermal history. The reversibility is caused by the free-energy renormalization arising from the large step entropy of highly stepped vicinal surfaces, which favors a flat 2D surface at higher temperatures, whereas the fully faceted nanostructured surface is the preferred low-temperature configuration. Because nanoripple growth is self-limited by the amount of material deposited, the nanoripple size is deterministically controlled by the Ge coverage and vicinal angle, which means that highly reproducible nanostructures with tunable geometries can be obtained. Our results reveal an astonishingly large surface mass transport taking place after growth during the cooldown process, leading in the extreme case to a complete restructuring of surface topography. This means that *postmortem* imaging of epitaxial surfaces does not always reveal actual morphologies of growth, which is an important factor to be taken into account. Last but not least, the generic nature of our results suggests that similar effects should occur for many other vicinal material systems. This opens up opportunities for realization of novel nanostructures for device applications.

## ACKNOWLEDGMENTS

We thank Istvan Daruka for developing the original free-energy model taking the step entropy into account. This work was supported by the Austrian Science Funds, Project No. P28185-N27, and the European Union's Horizon 2020 research and innovation program under Grant agreement No. 735008 (SiLAS).

## APPENDIX: SCALING INCLUDING INTERDIFFUSION AND A NONZERO WETTING LAYER

For the experimental scaling analysis of the nanoripple period as a function of Ge coverage using Eq. (1) we have assumed that there is no Si/Ge intermixing and no residual 2D wetting layer present underneath the ripples. Si/Ge intermixing reduces the Ge concentration  $c_{\text{Ge}} < 1$  within the

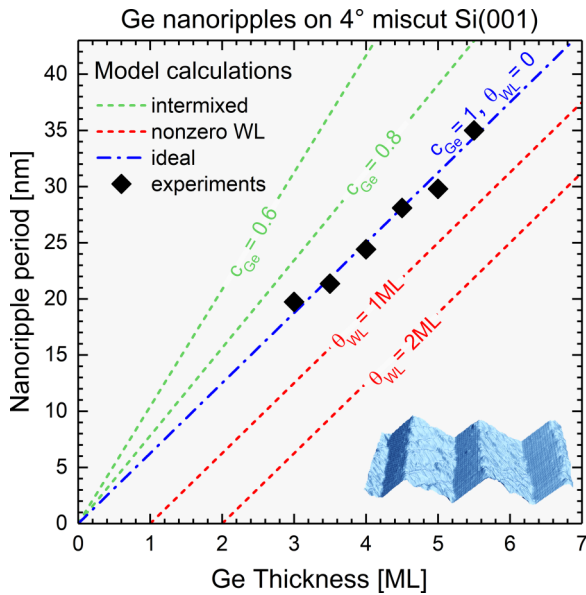


FIG. 10. Comparison between the experimental (diamonds) and theoretical nanoripple periods (dashed lines) as a function of Ge thickness for 4° vicinal Si(001) miscut towards the (100) direction. The dashed lines correspond to different model assumptions of: (i) pure Ge ripples without residual 2D wetting layer (blue dashed-dotted line), (ii) nanoripples with Si/Ge intermixing, i.e., reduced average Ge concentration of  $c_{\text{Ge}} = 0.6$  and  $0.8$  (dashed green lines), and (iii) nanoripples with a residual nonzero 2D wetting layer underneath with thickness  $\theta_{\text{WL}} = 1$  and  $2$  ML (dashed red lines). Clearly, the experimental data only fit well to the case when  $\theta_{\text{WL}} = 0$  and  $c_{\text{Ge}} = 1$ , as assumed in Eq. (1) of the main text.

ripples, which in term would increase the available volume of the ripple material. As a result, the ripple size and thus, the scaling parameter would be larger by a factor of  $1/c_{\text{Ge}}$  than for pure Ge nanoripples, i.e., the ripple period would increase more rapidly with the Ge coverage. On the contrary, the presence of a residual Ge wetting layer  $\theta_{\text{WL}}$  underneath the ripples would *reduce* the effective volume available for ripple formation, and thus the ripples size would be decreased. Both effects together yield a modified scaling relation of

$$p = 2h_{\text{ML}}(\cot \alpha + \cot \beta) \left( \frac{\theta_{\text{Ge}}}{c_{\text{Ge}}} - \theta_{\text{WL}} \right), \quad (\text{A1})$$

which in the limit of  $c_{\text{Ge}} = 1$  and  $\theta_{\text{WL}} = 0$  converges to Eq. (1) presented in the main text.

The modified scaling behavior for Ge on 4° miscut Si(001) is demonstrated by the dashed lines in Fig. 10, compared with the experimental data (black squares). For a finite residual wetting layer with  $\theta_{\text{WL}} = 1$  or  $2$  ML, evidently, the theoretical curves (red dashed lines) are shifted to higher coverages without change in slope, whereas for the case of Si/Ge intermixing reducing the Ge concentration in the ripples, e.g., to  $c_{\text{Ge}} = 0.6$  and  $0.8$  (green dashed lines in Fig. 10), the slope of the curves and thus, the scaling factor  $\lambda_{\alpha}$  substantially increases. As shown by Fig. 10, a good fit of the experimental data is obtained only for  $\theta_{\text{WL}} = 0$  and  $c_{\text{Ge}} = 100\%$  (blue dashed-dotted line), meaning that our original model assumptions hold for our experimental conditions. It is noted, however, that the perfect scaling applies only to the ripples formed during slow cooling through the 2D/ripple transition, where ripple formation is not limited by kinetic effects.

- [1] Z. Yuan, B. E. Kardynal, R. M. Stevenson, A. J. Shields, C. J. Lobo, K. Cooper, N. S. Beattie, M. Pepper, and M. Pepper, *Science* **295**, 102 (2002).
- [2] M. Sugawara and M. Usami, *Nat. Photonics* **3**, 30 (2009).
- [3] C. L. Salter, R. M. Stevenson, I. Farrer, C. A. Nicoll, D. A. Ritchie, and A. J. Shields, *Nature (London)* **465**, 594 (2010).
- [4] M. Müller, S. Bounouar, K. D. Jöns, M. Glässl, and P. Michler, *Nat. Photonics* **8**, 224 (2014).
- [5] P. Senellart, G. Solomon, and A. White, *Nat. Nanotechnol.* **12**, 1026 (2017).
- [6] D. Huber, M. Reindl, Y. Huo, H. Huang, J. S. Wildmann, O. G. Schmidt, A. Rastelli, and R. Trotta, *Nat. Commun.* **8**, 15506 (2017).
- [7] H. Watzinger, J. Kukučka, L. Vukušić, F. Gao, T. Wang, F. Schäffler, J.-J. Zhang, and G. Katsaros, *Nat. Commun.* **9**, 3902 (2018).
- [8] V. A. Shchukin and D. Bimberg, *Rev. Mod. Phys.* **71**, 1125 (1999).
- [9] C. Teichert, *Phys. Rep.* **365**, 335 (2002).
- [10] I. Berbezier and A. Ronda, *Surf. Sci. Rep.* **64**, 47 (2009).
- [11] J. Wu and P. Jin, *Front. Phys.* **10**, 7 (2015).
- [12] J. Stangl, V. Holý, and G. Bauer, *Rev. Mod. Phys.* **76**, 725 (2004).
- [13] M. Pinczolit, G. Springholz, and G. Bauer, *Appl. Phys. Lett.* **73**, 250 (1998).
- [14] M. Brehm, H. Lichtenberger, T. Fromherz, and G. Springholz, *Nanoscale Res. Lett.* **6**, 70 (2011).
- [15] G. Costantini, A. Rastelli, C. Manzano, R. Songmuang, O. G. Schmidt, K. Kern, and H. von Känel, *Appl. Phys. Lett.* **85**, 5673 (2004).
- [16] J. T. Robinson, D. A. Walko, D. A. Arms, D. S. Tinberg, P. G. Evans, Y. Cao, J. A. Little, A. Rastelli, O. G. Schmidt, and O. D. Dubon, *Phys. Rev. Lett.* **98**, 106102 (2007).
- [17] J.-N. Aqua, I. Berbezier, L. Favre, T. Frisch, and A. Ronda, *Phys. Rep.* **522**, 59 (2013).
- [18] G. Costantini, A. Rastelli, C. Manzano, P. Acosta-Diaz, G. Katsaros, R. Songmuang, O. G. Schmidt, H. v. Känel, and K. Kern, *J. Cryst. Growth* **278**, 38 (2005).
- [19] A. Raab and G. Springholz, *Appl. Phys. Lett.* **81**, 2457 (2002).
- [20] J. Tersoff and F. K. LeGoues, *Phys. Rev. Lett.* **72**, 3570 (1994).
- [21] X. L. Li, C. X. Wang, and G. W. Yang, *Prog. Mater. Sci.* **64**, 121 (2014).
- [22] I. Daruka, J. Tersoff, and A.-L. Barabási, *Phys. Rev. Lett.* **82**, 2753 (1999).
- [23] D. E. Jesson, G. Chen, K. M. Chen, and S. J. Pennycook, *Phys. Rev. Lett.* **80**, 5156 (1998).
- [24] F. M. Ross, J. Tersoff, and R. M. Tromp, *Phys. Rev. Lett.* **80**, 984 (1998).
- [25] T. I. Kamins, G. Medeiros-Ribeiro, D. A. A. Ohlberg, and R. Stanley Williams, *J. Appl. Phys.* **85**, 1159 (1999).

- [26] E. Placidi, A. Della Pia, and F. Arciprete, *Appl. Phys. Lett.* **94**, 021901 (2009).
- [27] L. Persichetti, A. Sgarlata, M. Fanfoni, and A. Balzarotti, *J. Phys.: Condens. Matter J.* **27**, 253001 (2015).
- [28] F. Watanabe, D. G. Cahill, S. Hong, and J. E. Greene, *Appl. Phys. Lett.* **85**, 1238 (2004).
- [29] B. Sanduijav, D. Matei, G. Chen, and G. Springholz, *Phys. Rev. B* **80**, 125329 (2009).
- [30] G. Chen, B. Sanduijav, D. Matei, G. Springholz, D. Scopece, M. J. J. Beck, F. Montalenti, and L. Miglio, *Phys. Rev. Lett.* **108**, 055503 (2012).
- [31] Z. Zhong, H. Gong, Y. Ma, Y. Fan, and Z. Jiang, *Nanoscale Res. Lett.* **6**, 322 (2011).
- [32] J.-h. Zhu, K. Brunner, G. Abstreiter, O. Kienzle, F. Ernst, and M. Rühle, *Phys. Rev. B* **60**, 10935 (1999).
- [33] T. Zhou, G. Vastola, Y.-W. Zhang, Q. Ren, Y. Fan, and Z. Zhong, *Nanoscale* **7**, 5835 (2015).
- [34] L. Du, D. Scopece, G. Springholz, F. Schäffler, and G. Chen, *Phys. Rev. B* **90**, 075308 (2014).
- [35] G. Chen, G. Springholz, W. Jantsch, and F. Schäffler, *Appl. Phys. Lett.* **99**, 043103 (2011).
- [36] J. J. Zhang, G. Katsaros, F. Montalenti, D. Scopece, R. O. Rezaev, C. Mickel, B. Rellinghaus, L. Miglio, S. De Franceschi, A. Rastelli, and O. G. Schmidt, *Phys. Rev. Lett.* **109**, 085502 (2012).
- [37] J. J. Zhang, A. Rastelli, O. G. Schmidt, D. Scopece, L. Miglio, and F. Montalenti, *Appl. Phys. Lett.* **103**, 083109 (2013).
- [38] L. Vukušić, J. Kukučka, H. Watzinger, J. M. Milem, F. Schäffler, and G. Katsaros, *Nano Lett.* **18**, 7141 (2018).
- [39] L. Vukušić, J. Kukučka, H. Watzinger, and G. Katsaros, *Nano Lett.* **17**, 5706 (2017).
- [40] F. Maier, J. Klinovaja, and D. Loss, *Phys. Rev. B* **90**, 195421 (2014).
- [41] B. Voigtländer, *Surf. Sci. Rep.* **43**, 127 (2001).
- [42] I. Goldfarb, P. T. Hayden, J. H. G. Owen, and G. A. D. Briggs, *Phys. Rev. Lett.* **78**, 3959 (1997).
- [43] E. D. Williams, *Surf. Sci.* **299–300**, 502 (1994).
- [44] H.-C. Jeong and E. D. Williams, *Surf. Sci. Rep.* **34**, 171 (1999).
- [45] H. J. W. Zandvliet, *Rev. Mod. Phys.* **72**, 593 (2000).
- [46] B. S. Swartzentruber, N. Kitamura, M. G. Lagally, and M. B. Webb, *Phys. Rev. B* **47**, 13432 (1993).
- [47] H. J. W. Zandvliet and H. B. Elswijk, *Phys. Rev. B* **48**, 14269 (1993).
- [48] H. J. W. Zandvliet, O. Gurlu, R. van Gastel, and B. Poelsema, *Phys. Rev. B* **69**, 125311 (2004).
- [49] O. G. Schmidt, U. Denker, S. Christiansen, and F. Ernst, *Appl. Phys. Lett.* **81**, 2614 (2002).
- [50] G. Capellini, M. De Seta, and F. Evangelisti, *Appl. Phys. Lett.* **78**, 303 (2001).
- [51] G. Katsaros, G. Costantini, M. Stoffel, R. Esteban, A. M. Bittner, A. Rastelli, U. Denker, O. G. Schmidt, and K. Kern, *Phys. Rev. B: Condens. Matter Mater. Phys.* **72**, 195320 (2005).
- [52] H. J. W. Zandvliet, *Phys. Rep.* **388**, 1 (2003).
- [53] M. A. Lutz, R. M. Feenstra, P. M. Mooney, J. Tersoff, and J. O. Chu, *Surf. Sci.* **316**, L1075 (1994).
- [54] P. Raiteri, D. B. Migas, L. Miglio, A. Rastelli, and H. von Känel, *Phys. Rev. Lett.* **88**, 256103 (2002).
- [55] G. Medeiros-Ribeiro, A. M. Bratkovski, T. I. Kamins, D. A. A. Ohlberg, and R. S. Williams, *Science* **279**, 353 (1998).
- [56] F. M. Ross, R. M. Tromp, and M. C. Reuter, *Science* **286**, 1931 (1999).
- [57] M. Brehm, F. Montalenti, M. Grydlik, G. Vastola, H. Lichtenberger, N. Hrauda, M. J. Beck, T. Fromherz, F. Schäffler, L. Miglio, and G. Bauer, *Phys. Rev. B* **80**, 205321 (2009).
- [58] M. Stoffel, A. Rastelli, J. Tersoff, T. Merdzhanova, and O. G. Schmidt, *Phys. Rev. B* **74**, 155326 (2006).
- [59] See Supplemental Material at <http://link.aps.org/supplemental/10.1103/PhysRevB.102.075420> for description of the growth rate calibration and of dome and pyramid formation at temperatures higher than 600 °C.
- [60] F. Montalenti, D. Scopece, and L. Miglio, *C. R. Phys.* **14**, 542 (2013).
- [61] G.-H. Lu and F. Liu, *Phys. Rev. Lett.* **94**, 176103 (2005).
- [62] M. J. Beck, A. van de Walle, and M. Asta, *Phys. Rev. B* **70**, 205337 (2004).
- [63] D. Scopece, F. Montalenti, and M. J. Beck, *Phys. Rev. B* **85**, 085312 (2012).
- [64] E. E. Gruber and W. W. Mullins, *J. Phys. Chem. Solids* **28**, 875 (1967).
- [65] E. D. Williams and N. C. Bartelt, *Science* **251**, 393 (1991).
- [66] H. J. W. Zandvliet, *Phys. Rev. B* **61**, 9972 (2000).
- [67] J. Tersoff and R. M. Tromp, *Phys. Rev. Lett.* **70**, 2782 (1993).
- [68] H. Hu and F. Liu, in *IUTAM Symposium on Surface Effects in the Mechanics of Nanomaterials and Heterostructures*, edited by A. Cocks and J. Wang (Springer, Dordrecht, 2013), pp. 59–70.
- [69] C. M. Retford, M. Asta, M. J. Miksis, P. W. Voorhees, and E. B. Webb, *Phys. Rev. B* **75**, 075311 (2007).
- [70] Y. Zhang and J. Drucker, *J. Appl. Phys.* **93**, 9583 (2003).
- [71] S. Song, S. G. J. Mochrie, and G. B. Stephenson, *Phys. Rev. Lett.* **74**, 5240 (1995).
- [72] K. Sudoh and H. Iwasaki, *Phys. Rev. Lett.* **87**, 216103 (2001).
- [73] M. Yoon, S. G. J. Mochrie, M. W. Tate, S. M. Gruner, and E. F. Eikenberry, *Phys. Rev. Lett.* **80**, 337 (1998).